5-1978

Experimental Measurements and Interpretation of Ultrasonic Scattering by Flaws

Bernard R. Tittmann

Experimental Measurements and Interpretation of Ultrasonic Scattering by Flaws

Abstract
Experimental measurements have been carried out in previous efforts on the scattering of elastic waves from ellipsoidal and spherical cavities embedded in titanium on alloy by the diffusion bonding process. The scattering data have been compared with calculations from exact theory and those from the Born approximation. The results demonstrated that the new concept of sample fabrication by the diffusion bonding process is successful, and that the approximate scattering models developed to date are both useful and correct within acceptable limits for many applications. Efforts have been expended this year to provide a scheme and useful data base for the development of inversion techniques (i .e., deterministic, probabilistic, or adaptive schemes) from which quantitative properties of the scattering center can be rapidly extracted. The work has provided a preliminary definition of the minimum quantity and type of data acquisition needed for a "smart" NDE system.

Keywords
Nondestructive Evaluation

EXPERIMENTAL MEASUREMENTS AND INTERPRETATION OF ULTRASONIC SCATTERING BY FLAWS

B. R. Tittmann and R. K. Elsley
Science Center, Rockwell International
Thousand Oaks, California 91360

ABSTRACT

Experimental measurements have been carried out in previous efforts on the scattering of elastic waves from ellipsoidal and spherical cavities embedded in titanium on alloy by the diffusion bonding process. The scattering data have been compared with calculations from exact theory and those from the Born approximation. The results demonstrated that the new concept of sample fabrication by the diffusion bonding process is successful, and that the approximate scattering models developed to date are both useful and correct within acceptable limits for many applications. Efforts have been expended this year to provide a scheme and useful data base for the development of inversion techniques (i.e., deterministic, probabilistic, or adaptive schemes) from which quantitative properties of the scattering center can be rapidly extracted. The work has provided a preliminary definition of the minimum quantity and type of data acquisition needed for a "smart" NDE system.

Introduction

The objective of the third year was a coordinated effort among the various investigators to integrate the results of all the studies into a demonstration of defect characterization capability. This has focused upon the problem of identifying the size, shape, and orientation of a spheroidal cavity embedded in a solid by inversion techniques. A part of the effort is focused on the utilization of the adaptive learning capabilities developed by Mucciardi at Adaptronics (see this proceedings) to develop predictive relationships inverting measured ultrasonic fields to obtain the geometric properties of the spheroidal cavities. Thus theoretical models developed by Krumhansl, Gubernatis, Domany, et al. (see this proceedings) were tested against the experimental data obtained in the contract mode on idealized spherically shaped samples in the study described in detail below and against data obtained in the immersion mode on samples with flat surfaces by Adler (see this proceedings).

Data Acquisition Plan for Inversion

A data acquisition plan was formulated to provide a base of experimental data for use in developing scattering inversion techniques (i.e., deterministic, probabilistic, or adaptive learning schemes). In order to simulate a realistic NDE situation, the plan limited the range of angles from which the defect could be "viewed" by the ultrasonic transducers. Each defect was located at the center of a sphere built in the form of a "trailer hitch" described below. A "viewing window" was defined on the surface of the sphere in terms of intersections of the surface with a cone centered on the defect and having a half-angle of 60° (see Fig. 1). The shaded area in Fig. 1(a) is the area within the viewing window. The window was placed at a variety of positions on the sphere to simulate defects of various orientations. Figure 1(b) is a stereographic projection of the viewing window. A grid of transducer positions is seen laid out in the window with circles indicating receiver positions and squares indicating transmitter positions. For a given window position and for each transmitter position within the window, the scattered ultrasound waveform is recorded at each of the 17 receiver positions (one of the receiver positions is the same as the transmitter position and the data is taken as a pulse echo measurement).

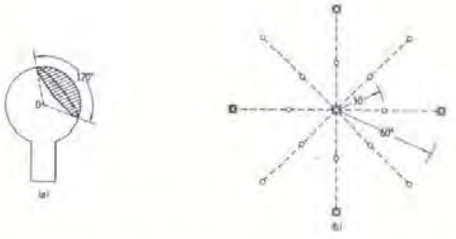

Figure 1. (a) "Trailer hitch" spherical sample with ellipsoidal void defect at center (D). Shaded area is "viewing window" available to ultrasonic transducers.

(b) Stereographic projection of viewing window showing receiver positions (circles) and transmitter positions (squares).

Sample Fabrication and Measurement Apparatus

As described in detail by Paton,[1] in the sample fabrication two cylinders of Ti alloy were machined and then their bases diffusion bonded together in such a way that the final longer cylinder contained a spheroidal cavity at its center. Then this cylinder was machined into a configuration of a sphere on a pedestal such as shown in Fig. 2 with the center of the defect coinciding with the center of the sphere. In this way ten (10) samples were fabricated, as listed in Fig. 2, with defect geometries, including prolate and oblate spheroids and thin discs. The motivation for machining the samples into a spherical configuration was to provide the simplest geometry possible for probing and

analyzing the three-dimensional far field scattering patterns for the obstacles with the goal of measuring phase as well as amplitude.

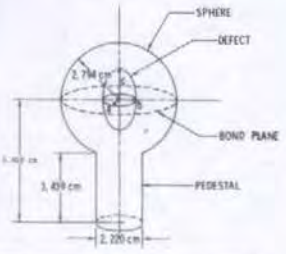

DESCRIPTION	a (μm)	b (μm)	c (μm)	STAMP NO.
PROLATE SPHEROID	200	200	800	40
PROLATE SPHEROID	400	400	800	41
SPHERE	800	800	800	35
SPHERE	400	400	400	36
SPHERE	600	600	600	37
OBLATE SPHEROID	400	400	200	39
OBLATE SPHEROID	400	400	100	38
CIRCULAR DISC	800	800	100	42
ELLIPTICAL DISC	2000	800	250	43
SIMULATED CRACK	600	600	-	47

Figure 2. Sample configuration and list of samples.

The measurement fixture, shown in Fig. 3, was designed and constructed to allow arbitrary motion of two transducers across the surface of the sphere, as well as another transducer mounted to the bottom of the pedestal. Figure 4 establishes the coordinate system for the various transducers with respect to the defect and defines the polar angle α and the azimuthal angle β for the two moving transducers.

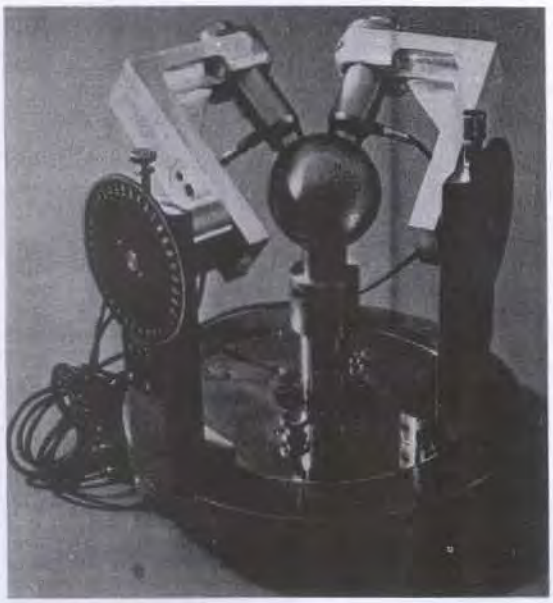

Figure 3. Photograph of sample holder.

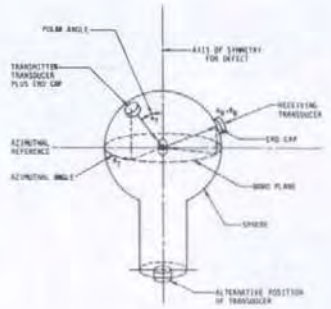

Figure 4. Measurement coordinate system.

The measurement apparatus is outlined in Fig. 5. The transducers used are 5 MHz broadband Panametrics units and are pulsed by either a UM721 Reflectoscope or a Panametrics 5052PR. The coupling between the flat transducer wear plates and the spherical sample surface was accomplished with the aid of end caps constructed from the same stock Ti-alloy as the sample and polished to conform to the mating surfaces. R.F. waveforms are captured by a Biomation 8100 transient recorder and the experiments are controlled and signal processing performed on an Eclipse mini-computer using the Science Center's Interpretive Signal Processor language. The frequency range studied has been chosen to be 2-10 MHz in order to give a range of ka = 0.5-10.

Scattering Data Base for Use in Inversion

With the techniques described above, scattering data were collected on defects for which the current theoretical approximation work the best, i.e., cavities in the shape of oblate spheroids. This data was added to the computerized ultrasonic scattering base at the Science Center and is available on 9-track 800 BPI magnetic tape for use in developing scattering inversion techniques. A copy of the data has been sent to Adaptronics, Inc., and is discussed by Mucciardi (see this proceedings).

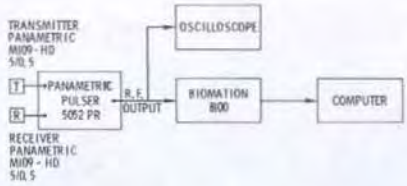

Figure 5. Schematic - Data Acquisition System.

Figure 6 shows a sample waveform and its Fourier transform (absolute value) on specimen No. 39 containing a cavity in the shape of an oblate spheroid. Complete sets of waveforms have now been obtained for four windows (see Fig. 1(b)) on each of two oblate spheroid samples (Nos. 38 and 39) for directly scattered longitudinal waves and are summarized in Table I.

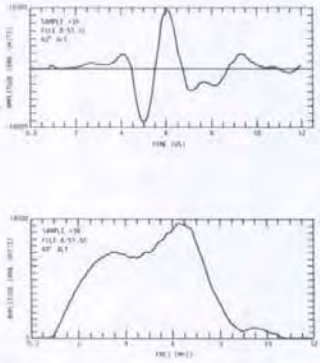

Figure 6. Sample waveform and its Fourier spectrum (magnitude) for pulse-echo data on oblate spheroid at a polar angle of 40° from axis of symmetry.

TABLE I

DEFECT SIZE AND ORIENTATION

ALIAS NAME	RADIUS ALONG AXIS (μm)	RADIUS PERP. AXIS (μm)	ELEV. (POLAR) ANGLE α	AZIM. ANGLE β
1Q	200	400	0	0
2Q	200	400	30	225
3Q	100	400	80	160
4Q	100	400	0	0
5Q	200	400	80	160
6Q	100	400	30	0
7Q	200	400	30	0
8Q	100	400	30	225

Figure 7 and 8 demonstrate some of the qualitative features in the data. In Fig. 7 the scattered waveform peak-to-peak amplitude is written in dB at each receiver site for a transmitter 60° away from the window axis, which in this case coincides with the axis of symmetry for the defect, an oblate spheroid with a 2 to 1 aspect ratio. Contour lines are indicated approximately in order to demonstrate how the radiation pattern for the scattered power appears to tilt away from the transmitter position, in agreement with intuition. In Fig. 8 similarly obtained data are plotted on a computer contour plot developed by Domany (see this proceedings) with reasonable agreement considering the 1 dB accuracy of the data (which corresponds to two integers on the contour plot).

Figure 7. Sample data from data set 1Q (see Table I) for transmitter positioned at (60°, 180°) the bottom of the window. The numbers are relative power in dB recorded by a receiver moved successively to the other window positions. The dashed lines are rough estimates for 12.0 dB, 10 dB, and 6.9 dB contours.

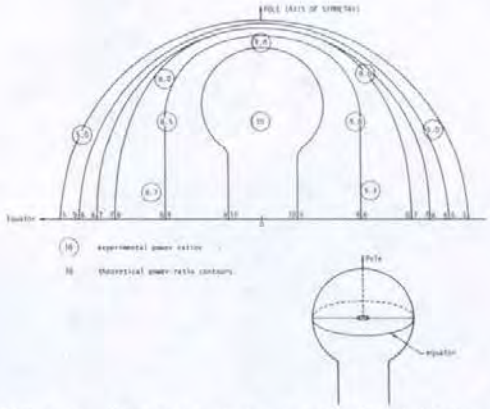

Figure 8. Comparison between calculated (from Born approximation) and observed power ratios for scattering from oblate spheroid No. 39. The results obtained for the surface of the spherical sample are plotted in the form of a projection (see Domany, this report). The transmitter is at "0". The maximum power scattered is arbitrarily chosen as 10.

Angular Dependence for Spheroidal Defects

A scatterer of irregular shapes reflects different amounts of sound in different directions. This makes possible the estimation of shape (i.e., "out-of-roundness") and orientation by observing the peak height of the pulse-echo video signal when the defect is viewed from a variety of directions.[2]

Figure 9 surveys some of the theoretical and experimental results in order to draw attention to the qualitative differences between the various defects.[3] The figure shows backscattered power as a function of the polar angle for a sphere, an oblate spheroid, a prolate spheroid and a circular disc. Both the experimental curves (dashed lines) and the theoretical curves (solid lines) are normalized along the symmetry axis (polar angle $\alpha = 0$). The theoretical curves are results of Born approximation calculations.

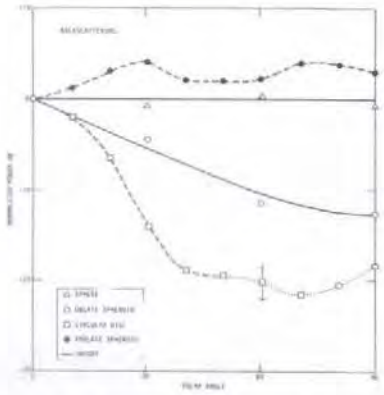

Figure 9. Angular dependence of pulse-echo power (data normalized at zero polar angle α).

The plot demonstrates the dramatic differences in the angular dependence for the various shapes when the sizes of the objects are approximately comparable. Measurement of the backscattered power for a few angles near $\alpha = 0$ is clearly sufficient to classify the scattering object according to shape. Furthermore, to the extent that quantitative calculations have been applied to the data at this time, good agreement between theory and experiment is observed. All the salient features of Fig. 9 are in quantitative agreement with the Born approximation, see Fig. 10 for the spheroidal shape and with Keller's theory for the discs (see Adler, this proceedings).

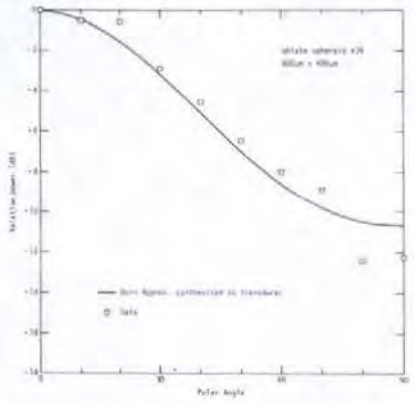

Figure 10. Comparison of pulse-echo data as a function of polar angle α with predictions of Born approximation. (The calculations take into account the transducer characteristics.)

Figure 11 presents more detailed results for a number of shapes and sizes in an unnormalized way and focuses attention on the quantitative differences between the defects. For example, the 600 μm radius sphere gives an approximately 4 dB higher backscattering than the 400 μm radius sphere. This is in agreement with physical intuition and in good quantitative agreement with scattering theory which scales the intensity by ρ^2 where ρ is the radius of curvature--(in this case $\rho = a$) and predicts a difference of 3.5 dB.

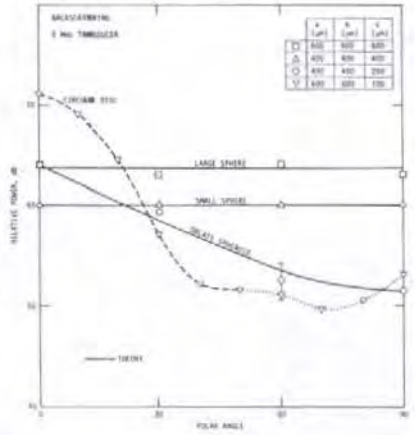

Figure 11. Angular dependence of pulse-echo power.

Figure 12 shows the angular dependence of the scattering from an elliptical disc. Large polar angle data are given in the form of dots instead of dashes to indicate the presence of pulse splitting; i.e., instead of a single echo pulse, two closely spaced echos were observed. The spacing between the pulses agrees well with that calculated on the basis that the near and far edges of the discs can, to first order, be treated as individual sources of scattered radiation which then arrive at the receiver along paths differing by about $2\ell \sin\ell$ where ℓ is the diameter of the disc in the plane traversed by the transducer. There are two key differences in the scattered radiation pattern: (1) the main lobe is narrower for traversal of the transducer in the plane of the major axis of the ellipse, because phase cancellation across the disc can occur at much smaller values for the polar angle than for the case of traversal across the minor axis; and, (2) the narrow lobe data (traversal across major axis) shows a lower side-scattered ($\alpha = 90^\circ$) power level, because the transducer at that angle faces the smaller cross section of the disc. Calculations predict a difference of 12.4 dB which is in good agreement with the observed $\approx$12 dB. These features, as well as the degree of splitting in the echo pulse, are thus seen to provide powerful indicators of the size and shape of defects approximating penny-shaped cracks. The lack of symmetry in the plots is thought to result from distortions of the disc-shaped cavity incurred during the bonding process.

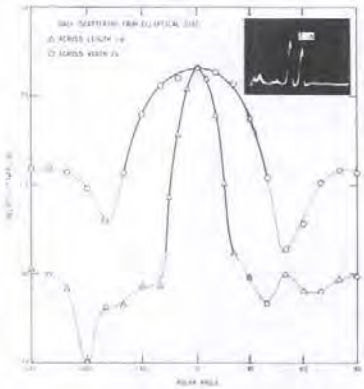

Figure 12. Angular dependence of pulse-echo power for disc. The dotted lines indicate regimes where double pulse (see insert) appears.

Figure 13 presents data obtained on the spheroidal cavities as a function of the aspect ratio. The measurement was in part motivated by calculations made available for this problem by the use of the Born approximation. The theoretical curve was obtained by averaging the calculations over $0 \leq kc \leq 2$, where k is the wave vector of the ultrasonic wave and 2c is the length of the ellipsoid axis in the direction of the incident wave. To accomplish a comparison with the available samples, a different transducer set (i.e., with different center frequency) had to be used with each sample. This ensured that kc would be approximately constant throughout the experiment. Furthermore, wide-band transducers were used so that some averaging could be accomplished approximating the theoretical averaging over the range of kc values described above. As seen in Fig. 13, the agreement between theory and experiment is good, and in view of the difficulties in the experiment, remarkably close. The significance of this study is that it allows a qualitative extrapolation to the case of the penny-shaped crack which is one of the geometries frequently encountered in commercial NDE applications.

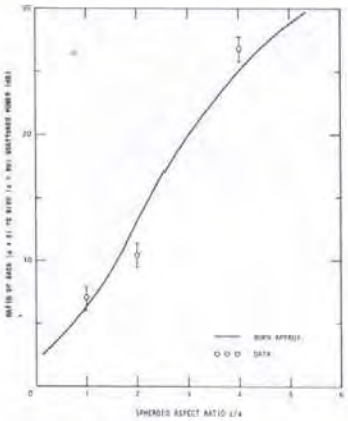

Figure 13. Ratio of back-scattered (pulse-echo) to side-scattered (pitch-catch) power.

Figure 14 presents preliminary data on the angular dependence of the pulse-echo peak height from a simulated crack 1200 μm in diameter. As described by Paton,[1] the defect was made by placing a small amount of non-metallic compound (yttria) on the mating surface and inhibiting the bonding process in that area. As expected, the measurements were very difficult to carry out because most of the signal passed through the flaw and special techniques of signal averaging yet to be developed are required to remove the competing signals from scattering off metallurgical second phases. Nevertheless, these preliminary data are interesting because they display a rapid roll-off at small polar angles (faster than the data for the circular disk of the same diameter) in good agreement with Adler's calculations from Keller's theory (see this proceedings).

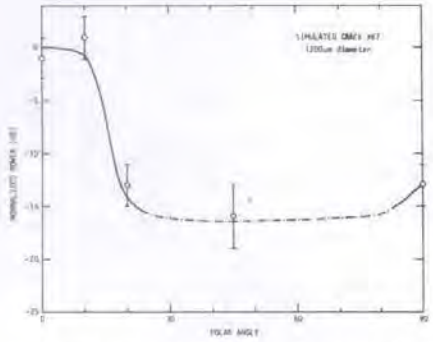

Figure 14. Angular dependence of pulse-echo power for simulated crack.

A number of measurements were carried out to see how the frequency dependence of pulse-echos (backscattering) from an oblate spheroid vary with polar angle. These data were obtained by spectrum analyzing the waveforms of broad-band pulse-echos. As reference, Fig. 15 presents the frequency dependence for longitudinal backscattering from a spherical cavity 800 μm in diameter and shows good agreement between experiment and classical scattering theory. Also shown in Fig. 15 (top graph) is the calculated frequency dependence for a sphere with half the diameter (400 μm). The key difference is that the graph appears to have been stretched out so that the oscillations exhibit a larger period and the first (low frequency) hump has been pushed to higher frequencies. This observation is equivalent to noting that the backscattering may be described by a single curve with ka as abscissa and that the first peak occurs at ka = 1. Because of the symmetry for the sphere, these results remain unchanged as a function of angle, and it is of interest to study the effects of deviation from symmetry.

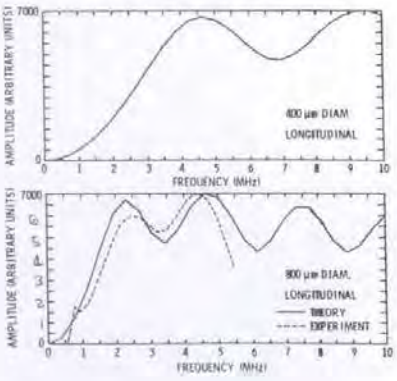

Figure 15. Comparison of "exact" theory and data for spherical void. The data is obtained by Fourier analyzing the pulse-echo waveform and dividing by transducer spectrum.

$$ka = \frac{2\pi a}{\lambda} = \frac{2\pi a f}{v}$$

$$= .299 f$$

Figure 16 shows representative data and calculations from approximate models for the backscattering from an oblate spheroid with a 2:1 aspect ratio (sample 39) at two polar angles $\alpha = 10^\circ$ and $\alpha = 60^\circ$. Among the main features noticeable is a qualitative similarity of Fig. 16 with Fig. 15, in that at low polar angles, the oblate spheroid behaves as if it had a small effective radius a, i.e., first peak at high frequencies, large period of oscillation. As the polar angle is allowed to increase, the frequency dependence changes smoothly--as if contracting--until at large polar angles, the location of the first (low frequency) peak and the period of oscillations suggest a large effective radius. To a limited extent this result is borne out by the approximate theoretical models in accurately predicting the location of the first (low frequency) peak, and suggests that angular dependence data could be used very effectively in determining the size of the flaw in addition to shape and orientation.

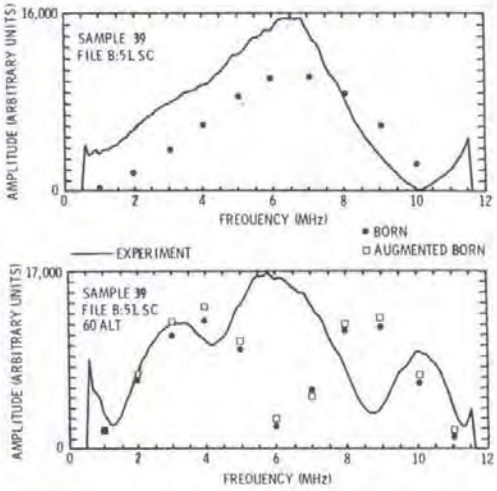

Figure 16. Comparison of approximate theories and data for back-scattering from an oblate spheroid for 10° (upper figure) and 60° (lower figure) off the axis of symmetry.

Time and Frequency Domain Analysis

A short ultrasonic pulse contains a wide band of frequencies. Because each frequency interacts differently with a defect, the scattered frequency spectrum is a signature of the defect. By studying the time-domain RF waveforms and the frequency spectra of the ultrasound backscattered from spherical scatterers, a number of techniques have been developed to determine size and impedance of the scatterers.

Waveforms - Figure 17 shows typical frequency spectral data. Figure 17 (upper left) shows the ultrasonic pulse produced by a broadband 5 MHz transducer. Figure 17 (upper right) shows the magnitude of the frequency spectrum of this pulse. Depending on the signal to noise ratio of the measurements, there is usable signal from 1 to 9 MHz. Figure 17 (middle left) shows the ultrasonic pulse which resulted when the above pulse was backscattered off of a 0.12 cm diameter spherical void in Ti-6Al-4V. The altered shape contains information about the scatterer. Figure 17 (middle right) shows the frequency spectrum of this scattered pulse. Here also there is structure characteristic of the scatterer. Finally, the effects of the transducer, pulser and medium can be removed by normalizing the scattered spectrum (middle right) by the pulse spectrum (upper right). This normalized spectrum is shown in Fig. 17 (lower right). Because of the small amount of energy present in the pulse at very low and very high frequencies, the normalization was cut off below 1/2 MHz and above 9 MHz. In the intervening region, the normalized spectrum is an accurate representation of the scattering properties of the defect.

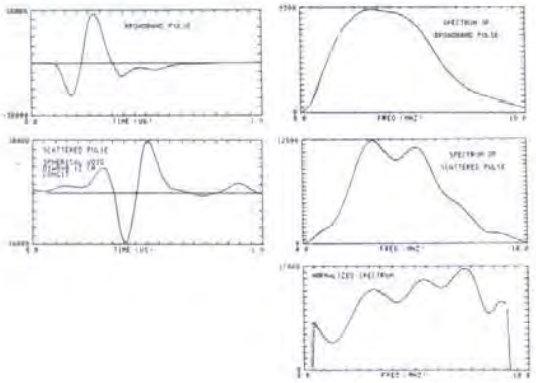

Figure 17. Time domain (left) and frequency domain (right) waveforms for a broadband ultrasonic pulse (top), the same pulse after scattering from a spherical void (middle), and after original pulse is normalized out of scattered pulse (bottom).

In order to find relationships between scattered signals and the properties of the scatterers, we have first studied theoretically calculated waveforms. For spherical voids and inclusions (though not for more complicated shapes), it is possible to calculate exactly the scattered ultrasonic waveforms. Calculations have been made using the method of Tittmann and Cohen for spherical scatters in a variety of sizes and material content.

Consider first the RF waveform. Figure 18(a) shows the backscattered waveform of a spherical void. It was calculated by first calculating the scattering as a function of frequency and then inverse Fourier transforming to obtain the waveform. The result is the response of the void to a pulse of the shape shown in Fig. 18(b) (a "Hanning pulse"). This pulse contains energy in a frequency range typical of ultrasonic NDE: 0 to 10 MHz. It differs from actual ultrasonic pulses in that it contains energy down to very low frequencies, which is an aid in searching for useful relationships in the scattering data.

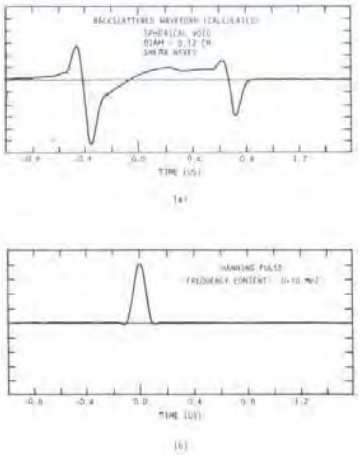

Figure 18. (a) Calculated time-domain response of 0.12 cm diameter spherical void to incident hanning pulse.
(b) Hanning pulse.

At high frequencies, the front surface of the void will be approximately flat over an area several wavelengths across and will therefore reflect a substantial amount of sound. At low frequencies, on the other hand, the front surface will be only a fraction of a wavelength across and will reflect little. In Fig. 18(a), T=0 is at the center of the defect. At T=-0.4 US, there is pulse consisting of a negative and a positive peak. It is a copy of the input Hanning pulse, at the time of the front surface, with its low frequency energy missing.

Other energy will be scattered at later times as the defect responds to the incident sound pulse. In the case of the void shown in Fig. 18(a), there is a well defined second pulse at T=0.65 US.

The frequency spectrum of the void is shown in Figs. 19 and 20. Figure 19 shows the magnitude spectrum. At low frequencies there is, as expected, little energy. At high frequencies, the interference of the two pulses causes a characteristic oscillation whose period is inversely proportional to the size of the void.

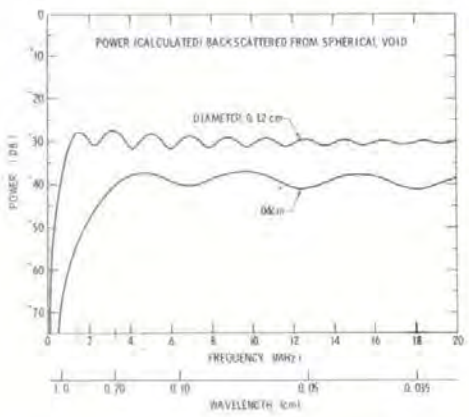

Figure 19. Calculated pulse-echo magnitude spectra for two spherical void scatterers.

The phase spectrum is shown in Fig. 20. To interpret the phase spectrum, recall that the effect of varying the arrival time of a pulse is to add to the phase spectrum a ramp of the form $\theta = 2\pi fT$ where T is the arrival time.

Figure 20 shows an upward slope corresponding to the arrival time of the front surface echo. The oscillations on this ramp are caused by the arrival time of the second echo. At low frequencies, the slope is zero, indicating that long wavelengths sense primarily the enter of the defect (T = 0).

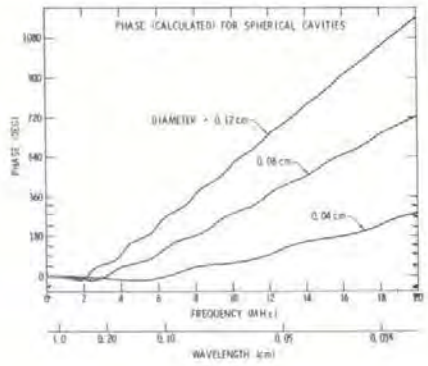

Figure 20. Calculated phase spectrum of 0.12 cm, 0.08 cm, and 0.04 cm diameter spherical void. Upward slope at high frequencies indicates that front face of void is nearer than its center. Flat slope at low frequencies indicates position of center.

$ka = \frac{2\pi a}{v} f = .1995 f$ for .04 cm - 2a

Because the frequency spectrum stretches and shrinks, but does not change shape as the size of a scatter of fixed shape varies, the frequency of any feature of the frequency spectrum could be used as a measure of size. Thus, for longitudinal wave inspection of spherical voids, the first or second peaks of the magnitude spectrum predict diameter via the following relationships:

First peak:

$$\text{diam (mils)} = \frac{74.25 \text{ mils} * \text{MHz}}{\text{Frequency}}$$

Second peak:

$$\text{diam (mils)} = \frac{150.9 \text{ mils} * \text{MHz}}{\text{Frequency}}$$

Applying these formulae to experimentally measured spectra yields the following estimates:

Actual Diameter	Estimated Diameter	Difference
31.5	30.0	5%
47.24	47.13	1/4%

For a tungsten carbide sphere in Titanium-6-4, the first peak of the spectrum predicts diameter according to:

First peak:

$$\text{diam (mils)} = \frac{127 \text{ mils} * \text{MHz}}{\text{Frequency}}$$

For an experimental spectrum:

Actual Diameter	Estimated Diameter	Difference
31.5	31.36	1/2%

A more systematic approach is to measure the period of the oscillations of the magnitude spectrum by calculating a spectrum and noting the position of its maximum. This approach will be limited for very small defects, where the spectrum will consist of only the first part of Fig. 19 and there will be no oscillations to measure. As reported in the second annual report, this technique should give 30% accurate estimates down to diameters as small as 1/2 wavelength of sound.

The features of the spectrum which have been used in the preceding paragraphs are not independent of the material contained within the sphere. A technique which promises to be material independent makes use of the phase spectrum and is based on the following strategy:

1) Locate the front surface of the defect using high frequencies (short wavelengths)

2) Locate the center using low frequencies (long wavelengths)

3) Subtract (1) from (2) to find defect size.

It was noted above that the high frequency part of the phase spectrum has a slope which indicates the location of the front surface of the defect, while the low frequency part has a slope which indicates the position of the center. Therefore, the difference of the slopes indicates size:

Diameter = velocity in host medium x

$$\frac{1}{4\pi}\left(\left.\frac{d\phi}{df}\right|_{\text{low freq.}} - \left.\frac{d\phi}{df}\right|_{\text{high freq.}}\right)$$

This method is independent of the material included within the defect and independent of the shape of the defect.

Figure 21 shows the results for experimental data from an oblate spheroid of semi-axes 100 and 400 microns viewed along the 100 micron axis. The phase slope method predicts a semi-axis of 114μm, in excellent agreement with the actual value of 100μm.

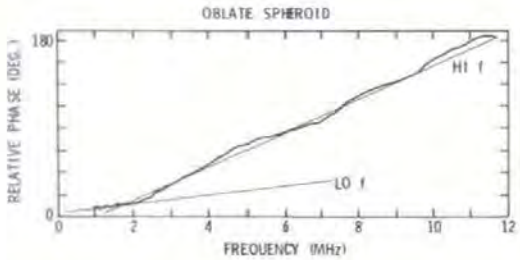

$$\text{HI: } \frac{d\phi}{df} = \frac{3.4\ \text{rad}}{11\ \text{MHz}} \qquad \tau_{HI} = \frac{1}{4\pi}\frac{d\phi}{df} = .0246\ \mu\text{sec}$$

$$\text{LO: } \frac{d\phi}{df} = \frac{1\ \text{rad}}{2\ \text{MHz}} \qquad \tau_{LO} = .0066\ \mu\text{sec}$$

$$\tau_{HI} - \tau_{LO} = .018\ \mu\text{sec} \qquad R = v\Delta\tau = .0114\ \text{cm}$$

Figure 21. Observed phase spectrum for back-scattering from oblate spheroid cavity along axis of symmetry and calculation of minor axis.

Finally, a technique has been developed which estimates the acoustic impedances of spherical solid inclusions in solids. It is based on the idea that the front surface of the scatterer is approximately flat, at least over a suitably small area. Therefore, when a pulse of ultrasound first encounters the scatterer, it will reflect in a manner similar to the way it would from a flat semi-infinite slab of the included material. By treating the back-scattered sound pulse as if it were reflecting from such a slab, an estimate of the inclusion impedance is arrived at using the equation

$$R = \frac{Z_H - Z_I}{Z_H + Z_I}$$

where: R is the reflection coefficient of acoustic displacement, Z_H is the impedance of the host medium, Z_I is the impedance of the inclusion.

A special case of this technique is that merely by noting the sign of the reflected pulse, it can be determined whether the inclusion has an impedance greater than or less than that of the host medium.

In order to see if the leading edge of a reflected pulse can be treated as the reflection from a plane even when the front surface of the scatterer has a large curvature (e.g., for a small scatterer), and even when only a limited range of frequencies is available, theoretically calculated waveforms have been used to make estimates of the longitudinal and transverse impedances of spherical (1.2 mm dia.) aluminum, brass, and tungsten carbide inclusions in Ti-6-4. The procedure consisted of using theoretically calculated frequency spectra covering the range 0 MHz to 10 MHz to construct the (time domain) reflected pulse that would result from an incident Hanning pulse which contains energy from 0 MHz to 10 MHz. To estimate the impedance of an inclusion, we need the reflection coefficient from its front surface. For this, we have used the height of the first peak of the waveform divided by the height of the first peak of the waveform from a void. In Fig. 18(a), this peak is the positive going one at t = -0.45μs. The accuracy of impedance estimates made using this technique is shown below.

Material	Error: Longitudinal Impedance	Error: Shear Impedance
Al	-3.6%	-9.5%
Brass	2.1%	-14.7%
WC	10.4%	-2537.0%

With one notable exception (which is not yet understood), the estimates are accurate to within 20%, even though the inclusion diameters are only twice the wavelength of the ultrasound.

The primary limitation of this technique is that it requires an absolute measurement of the scattered acoustic amplitude, and a knowledge of the inclusion diameter. The test to which the method has thus far been put is limited by the lack of noise (electrical or metallurgical) in the data, the absence of the band limiting effects of an ultrasonic transducer, and the application of the method only to spheres. It is expected that the addition of these factors will degrade the results somewhat, but not invalidate the technique.

Conclusions

One of the challenges facing ultrasonic NDT is the need to quantitatively evaluate defects so as to reduce the number of parts rejected unnecessarily. It is, therefore, desirable to obtain accurate measure of size, shape, orientation, and content of defects. To do this, we should collect as much information as needed and process that information by suitable methods. With this goal in mind, we have investigated small voids and inclusions of simple shapes in solids. The diffusion bonding process has been found most useful and has been used to make Ti-6-4 samples containing voids in the shape of spheres, ellipsoids of revolution, and disks. The r.f. waveforms of ultrasound scattered from these defects have been captured in real time and processed by a digital computer. With the aid of theoretical models based on both exact and Born approximation methods, signal processing algorithms have been developed which rapidly estimate, from experimental data, the geometrical properties of defects. The use of signal processing techniques on ultrasonic NDE waveforms can reveal much about the nature of small scatterers within a part. Angular dependence of the scattering gives information about the shape and orientation of the scatterer. Frequency analysis of pulse echo signals provides techniques for estimating the size and material content of the scatterers. Several of these techniques have been tested to void defects in titanium and show high promise of being usable in practical NDE applications. The work may be summarized by concluding that the new techniques in sample fabrication, measurement procedures, and data processing have provided a preliminary definition of the minimum quantity and type of data acquisition needed for a "smart" NDE system. The work has provided a useful data base for use in developing scattering inversion techniques (i.e., deterministic, probabilistic, or adaptive schemes) from which quantitative properties of the scattering center can be rapidly extracted. The scattering data have been found to be a valuable test for the evaluation and refinement of scattering theories which treat scattering from ellipsoidal cavities on an approximate basis. These results have been possible primarily because the new concept of sample fabrication by the diffusion bonding process was proven to be successful.

Acknowledgement

This research was sponsored by the Center for Advanced NDE operated by the Science Center, Rockwell International, for the Advanced Research Projects Agency and the Air Force Materials Laboratory under contract F33615-74-C-5180.

References

1. "Interdisciplinary Program for Quantitative Flaw Definition, Special Report Third Year Effort," Rockwell International Science Center, pp. 59-62.

2. R. K. Elsley and B. R. Tittmann, NDT Conference Proceedings (Southwest Research Institute, San Antonio, Texas, 1977), in press.

3. B. R. Tittmann, Proc. of 1976 IEEE Ultrasonics Symposium, IEEE Catalog #76 CH 1120-5SU, 74, 74-79 (1976).